

CONTENTS

LIST OF FIGURES	XVII
LIST OF TABLES	XXII
ABBREVIATIONS	XXIII
LIST OF SYMBOLS	XXV
PREFACE.....	XXXI

CHAPTER 1: INTRODUCTION AND LITERATURE REVIEWError! Bookmark not defined.

1.1	Background and Motivation	3
1.2.	Classification of Microwave Devices	6
1.3.	Gyrotron Oscillator	8
1.3.1.	Dispersion Relation.....	9
1.3.2	CRM Interaction Mechanism	10
1.3.3.	Operating Principle	14
1.3.4.	Schematic and Working	15
1.4.	Dynamic Nuclear Polarizatio and Nuclear Magnetic Resonance	Error!
	Bookmark not defined.	
1.5.	DNP / NMR Gyrotrons	18
1.6.	Current Effort	Error! Bookmark not defined. 1
1.7.	Plan and Scope.....	Error! Bookmark not defined. 3

CHAPTER 2: MULTIMODE THEORY OF GYROTRON OSCILLATORS..... 27

2.1.	Introduction	29
2.2.	Multimode Theory.....	32
2.3.	Design Methodology and Limiting Constraints	43
2.3.1	Mode Selection	44
2.3.2	Cavity losses	44
2.3.3	Voltage depression and Limiting Current	46
2.3.4	Start Oscillation Current.....	48

2.4.	Results and Discussion	52
2.4.1	Design procedure of 260 GHz Gyrotron	53
2.4.1.a	RF Interaction Structure	53
2.4.1.b	Cavity Field Profile	53
2.4.1.c	Coupling Coefficient	55
2.4.2	Numerical Benchmarking	56
2.5.	Conclusion.....	57
CHAPTER 3:	PIC SIMULATION, MAGNETIC AND THERMAL TUNING STUDIES OF MILLIMETER-WAVE GYROTRON.....	59
3.1.	Introduction	61
3.2.	Descriptions of PIC Simulation	63
3.3.	PIC Simulation of 260 GHz Gyrotron Cavity.....	66
3.3.1	Modelling and Beam-wave Interaction Process	64
3.3.2	PIC Simulation Results	67
3.4.	Thermal Study of Gyrotron cavity	69
3.5.	Continuous Frequency Tuning of Millimeter-Wave Gyrotron	71
3.5.1	Magnetic Tuning Scheme.....	74
3.5.2	Thermal Tuning Scheme	77
3.6.	Output System of the Gyrotron.....	80
3.6.1	RF Output Window.....	80
3.6.2	Electron Beam Depressed Collector	82
3.7.	Conclusion.....	83
CHAPTER 4:	DESIGN AND SIMULATION STUDIES OF MILLIMETER-WAVE GYROTRON USING METAL PBG RF CAVITY	85
4.1.	Introduction	87
4.2.	Design Methodology of the PBG Cavity.....	89
4.2.1	Dispersion Relation and Global Band Diagram	89
4.2.2	Mode Analysis.....	90

4.2.3	PBG Cavity Design	92
4.3.	Cold Analysis of PBG Cavity.....	93
4.3.1	Time Domain Analysis.....	93
4.3.2	Eigenmode Analysis	94
4.4.	Calculation of Quality Factor.....	96
4.5.	Design and PIC Simulation of PBG Gyrotron	97
4.5.1	Modelling of PBG Gyrotron.....	97
4.5.2	PIC Simulation of PBG Gyrotron	101
4.6.	Tuneability of PBG Gyrotron	102
4.7.	Thermal and Structural Analysis of PBG Cavity	104
4.8.	Conclusion	106
CHAPTER 5: DESIGN AND SIMULATION STUDIES OF GYROTRON USING MULTI-SECTION SLIGHTLY TAPERED RF CAVITY		
109		
5.1.	Introduction.....	111
5.2.	Design of Multi-Section Cavity	112
5.2.1	Diffraction Quality Factor and Resonating Frequency.....	112
	Error! Bookmark not defined.	
5.2.2	Cavity Field Profile.....	116
5.2.3	Effective Length, Total Quality Factor and Start Oscillation Current	119
5.3.	PIC Simulation of Multi-Section Cavity Gyrotron	121
5.4.	Thermal and Static Structural Analysis.....	122
5.5.	Tuneability of Multi-Section cavity Gyrotron.....	124
5.5.1	Magnetic Tuning Scheme	124
5.5.2	Thermal Tuning Scheme.....	127
5.6.	Discussion on Fabrication Aspects of the Cavity	128
5.7.	Conclusion.....	129
CHAPTER 6: SIMULATION INVESTIGATIONS OF SECOND HARMONIC SUBMILLIMETER-WAVE GYROTRON		
131		

6.1.	Introduction	133
6.2.	Modelling of Gyrotron	Error! Bookmark not defined. 134
6.2.1	Magnetron Injection Gun	134
6.2.2	Cavity Field Profile.....	135
6.2.3	Coupling Coefficient and Start Oscillation Current.....	136
6.3.	Multimode Simulation of Submillimeter-Wave Gyrotron.....	137
6.4.	Thermal and Static Structural Analysis	138
6.5.	Tuneability of Submillimeter-Wave Gyrotron.....	141
6.5.1	Magnetic Tuning Scheme.....	141
6.5.2	Thermal Tuning Scheme	143
6.6.	Output System	146
6.6.1	RF Window	146
6.6.2	Output Collector	146
6.7.	Conclusion.....	148
CHAPTER 7:	SUMMARY, CONCLUSION AND FUTURE SCOPE.....	149
7.1.	Summary and Conclusion	151
7.2.	Limitations of the Present Work and Scope for Further Studies.	Error! Bookmark not defined. 156
	<i>References</i>.....	157
	<i>Author's relevant publications</i>.....	171

LIST OF FIGURES


Figure 1.1	Comparison of average power versus frequency for various types of devices	4
Figure 1.2	Classification chart of vacuum electron devices	6
Figure 1.3	Dispersion diagram of gyrotron oscillator	10
Figure 1.4	RF electric field of TE _{0n} mode with electron beamlets	10
Figure 1.5	Illustration of phase bunching phenomenon in an annular electron beam (a) random distribution, and (b) phase bunched electrons in their cyclotron orbits	12
Figure 1.6	Time evolution of electrons phase distribution (shown as ) in the Larmor orbit	13
Figure 1.7	Schematic arrangement of a gyrotron oscillator	15
Figure 2.1	The arrangement of electrons in the Larmor orbit with cylindrical coordinates and Cartesian coordinates	32
Figure 2.2	Radial profile and cavity field profile along the axial length of the cavity	54
Figure 2.3	(a) Relation between the coupling coefficient and normalized beam radius, and (b) SOC of TE _{7,2} mode and competing modes	55
Figure 2.4	The output power of operating TE _{7,2} mode and other competing modes using Multimode code (For beam parameters $V_b = 15.5$ keV, $I_b = 0.1$ A, $B_o = 9.52$ T and $\alpha = 1.12$)	57
Figure 3.1	Boundary conditions implementations around the RF interaction cavity	65
Figure 3.2	CST model of the gyrotron cavity	66
Figure 3.3	Particle preview of electron beam at the input side and at the output side	67
Figure 3.4	(a) Particle energy of the electron beam (b) fraction of the particle energy	67
Figure 3.5	(a) Amplitude of port signals, (b) power of TE _{7,2} mode, (c) frequency spectrum of the port signal of TE _{7,2} mode and (d) theoretically calculated power	68
Figure 3.6	(a) ANSYS model of the RF interaction cavity, (b) Heat transfer coefficient with a hydraulic diameter for different water flow rates in the grooves	69
Figure 3.7	(a) The temperature and deformation of the inner surface of straight section of the cavity, (b) the resonating frequency with respective water flow rate and shifting in resonating frequency at corresponding water flow rate at 290K	72
Figure 3.8	(a) The temperature distribution in the cavity, and (b) the total deformation of the cavity at coolant temperature 290K	72
Figure 3.9	The smooth transition between the $q = 1$ -like mode and $q = 2$ -like mode	73
Figure 3.10	SOC for axial mode number $q = 1 - 6$	74

Figure 3.11	The cavity field profile for axial mode number $q = 1 - 6$	76
Figure 3.12	The spectrum of the E-field monitors at the frequency (a) 260.46 GHz, (b) 260.69 GHz, (c) 261.05 GHz, and (d) 261.57 GHz	76
Figure 3.13	(a) Power Vs magnetic field (b) resonating frequency with the respective magnetic field (beam parameters are 15.5 kV, 100 mA, $\alpha = 1.12$, and total velocity spread is 2%)	77
Figure 3.14	Power Vs magnetic field for various velocity spread (beam parameters are 15.5 kV, 100mA, and $\alpha = 1.12$)	78
Figure 3.15	(a) Deformation distribution in the cavity and (b) The total quality factor (Q_T) and ohmic quality factor (Q_Ω) at the respective temperature	78
Figure 3.16	(a) Power versus magnetic field for thermal tuning and magnetic tuning and (b) Frequency versus magnetic field for thermal tuning and magnetic tuning	80
Figure 3.17	Transmission and reflection characteristics of single disk Sapphire window at $\epsilon_r = 9.394$ and loss tangent $\tan(\delta) = 4.5 \times 10^{-4}$	81
Figure 3.18	The temperature distribution of the collector	83
Figure 4.1	Metal PBG structures (a) unit cell in the triangular lattice (b) reciprocal lattice and Brillouin's zone (shaded area)	90
Figure 4.2	(a) Plot of normalized frequency verses peaks at certain location in the unit cell, (b) dispersion curve at $r/a = 0.40$	90
Figure 4.3	Global band-gap of the PBG cavity, where ● denotes the operating point	90
Figure 4.4	The relation between r/a and fa/c of different modes those confines in the defect after removing nineteen rods and shaded regions are the global bandgap	92
Figure 4.5	(a) Model of PBG cavity (b) S-Parameters of $TE_{7,2}$ -like mode	93
Figure 4.6	Boundary condition around the PBG cavity in the Eigenmode analysis	95
Figure 4.7	(a) E- field pattern of the $TE_{7,2}$ mode in the conventional cavity and (b) $TE_{7,2}$ -like mode in the PBG cavity	95
Figure 4.8	(a) Spectrum of the probed E-field, and (b) Stored energy decay	96
Figure 4.9	(a) Model of PBG gyrotron (b) normalized field profile with the radius of the gyrotron cavity	98
Figure 4.10	Confined frequencies in the PBG cavity with respective cells per wavelength	99
Figure 4.11	(a) Relation between coupling coefficient and normalized beam radius (b) SOC of $TE_{7,2,1}$ mode and its nearby competing modes	99
Figure 4.12	(a) Amplitudes of port signals (b) power in $TE_{7,2,1}$ -like mode (c) frequency spectrum of the port signal of $TE_{7,2,1}$ -like mode (d) output power through Multimode time-dependent calculation. The beam parameters 15.5kV, 140mA, and $\alpha = 1.7$ with 2% velocity spread are considered in the PIC simulation and Multimode simulation	100

Figure 4.13	Axial electric field variation inside the cavity in absence of electron beam, for (a) $q = 1$ (b) $q = 2$ (c) $q = 3$ and (d) $q = 4$	103
Figure 4.14	Comparison of (a) power and (b) frequency / bandwidth of PBG gyrotron and conventional gyrotron over magnetic field using PIC simulation and Multimode code (PBG gyrotron) for $V_0 = 15.5$ keV, $I_0 = 140$ mA, and $\alpha = 1.7$ with 2 % velocity spread.	104
Figure 4.15	Temperature (a) profile in the PBG cavity and (b) distribution in the radial direction	106
Figure 4.16	Deformation of rods in the PBG cavity (a) inner layer (b) middle layer (c) outer layer (d) E-field pattern resonating at 260.324 GHz	106
Figure 5.1	(a) Resonant frequency V_s taper angle θ_2 , and (b) diffractive Q factor V_s taper angle θ_2 for different taper length L_2 of $TE_{7,2,1}$ mode [for $L_4 = 0$, $\theta_4 = 0$, $\theta_3 = 0$, $L_1 = 10$ mm, $L_3 = 22$ mm, $L_5 = 10$ mm, and $L_6 = 63$ mm]	113
Figure 5.2	(a) Resonant frequency V_s taper angle θ_4 , and (b) diffractive Q factor V_s taper angle θ_4 for different taper length L_4 of $TE_{7,2,1}$ mode [for $L_2 = 0$, $\theta_2 = 0$, $\theta_3 = 0$, $L_1 = 10$ mm, $L_3 = 22$ mm, $L_5 = 10$ mm, and $L_6 = 63$ mm]	113
Figure 5.3	Resonant frequency and diffractive Q factor Q_d V_s taper angle θ_3 of $TE_{7,2,1}$ mode [for $L_2 = 0$, $\theta_2 = 0$, $L_4 = 0$, $\theta_4 = 0$, $L_1 = 10$ mm, $L_3 = 22$ mm, $L_5 = 10$ mm, and $L_6 = 63$ mm]	113
Figure 5.4	Cavity field profile and radial profile of the multi-section cavity	116
Figure 5.5	Cavity field profile for $TE_{7,2,q}$ mode (a) $q = 2$, (b) $q = 3$, (c) $q = 4$, (d) $q = 5$, (e) $q = 6$, (f) $q = 7$, (g) $q = 8$, and (h) $q = 9$	117
Figure 5.6	Comparison of the cavity field profile between the three-section cavity and multi-section cavity	118
Figure 5.7	Cavity field profile for (a) $q = 1$, (b) $q = 2$, (c) $q = 3$, (d) $q = 4$, (e) $q = 5$, (f) $q = 6$, (g) $q = 7$, (h) $q = 8$, and (i) $q = 9$ [for $\theta_2 = 0$, $\theta_3 = 0$, $\theta_4 = 0$, $L_2 = 12$ mm, $L_4 = 12$ mm, $L_1 = 10$ mm, $L_3 = 22$ mm, $L_5 = 10$ mm, and $L_6 = 63$ mm]	119
Figure 5.8	SOC for the $TE_{7,2,q}$ mode ($q = 1$ to 9)	120
Figure 5.9	(a) Amplitudes of port signals (b) power in $TE_{7,2}$ mode (c) frequency spectrum of the port signal of $TE_{7,2}$ mode (d) output power through Multimode time-dependent calculation. The beam parameters 15.5kV, 100 mA, and $\alpha = 1.12$ with a 2% velocity spread are considered in the PIC simulation and Multimode simulation	122
Figure 5.10	(a) Temperature distribution of cavity, (b) deformation distribution of cavity, and (c) temperature profile of the internal surface of the cavity and field profile of the cavity	123
Figure 5.11	The start oscillation current of $TE_{7,2,1}$ mode with other competing modes field (for the beam parameters 15.5 kV, 100 mA, $\alpha = 1.12$)	125
Figure 5.12		

Figure 5.13	(a) Power Vs magnetic field, and (b) resonating frequency with the corresponding magnetic field (for the beam parameters 15.5 kV, 100 mA, $\alpha = 1.12$, and velocity spread is 2 %)	126
Figure 6.1	(a) Power Vs magnetic field, and (b) resonating frequency with the respective magnetic field at the respective coolant (water) temperature	128
Figure 6.2	Model of MIG with electron beam profile and magnetic field profile	135
Figure 6.3	Velocity ratio (α) and velocity spread with respect to (a) modulating cathode voltage and (b) compression ratio (F_m)	135
Figure 6.4	Normalized cavity field profile and radial profile of the cavity	136
Figure 6.5	(a) Coupling coefficient and (b) start oscillation current of $TE_{11,2,1}$ mode along with other competing modes	137
Figure 6.6	Output power in operating $TE_{11,2}$ mode along with competing modes	138
Figure 6.7	(a) Cavity inner surface temperature and inner surface temperature with respective water flow rate and (b) resonant frequency, and shifting in resonating frequency of the cavity with respective water flow rate	139
Figure 6.8	(a) Temperature distribution of the cavity, (b) deformation distribution of the cavity with the coolant (water) temperature 290 K, and 0.7 L /m fluid flow between the grooves	140
Figure 6.9	SOC of the $TE_{11,2,q}$ mode with axial mode number $q = 1 - 4$	142
Figure 6.10	The cavity field profile for axial mode number $q = 1 - 4$	142
Figure 6.11	(a) Power Vs magnetic field (b) resonating frequency with respective magnetic field (beam parameters are 16.75 kV, 90 mA, $\alpha = 1.8$, and total velocity spread is 3%)	143
Figure 6.12	(a) Temperature distribution and (b) deformation distribution at the inner surface of the cavity for different coolant temperatures along the axial length of the cavity	144
Figure 6.13	(a) Power and (b) resonant frequency with respect to B-field for both thermal and magnetic tuning schemes	145
Figure 6.14	Transmission and reflection characteristics of the single disk Fused Quartz window at $\epsilon_r = 3.78$, $\tan(\delta) = 6 \times 10^{-5}$	147
	Temperature distribution of the collector	147

LIST OF TABLES

Table 1.1	State-Of-The-Art of the DNP/NMR Gyrotrons	20
Table 2.1	Structural and Electrical Parameters of the Gyrotron	52
Table 3.1	Properties of OFHC-Cu material at 290 K	68
Table 3.2	Quality factors and fr for axial mode number ($q = 1 - 6$)	74
Table 4.1	Resonating frequency and quality factor of RF cavities	95
Table 4.2	Design Parameters of PBG Gyrotron	100
Table 4.3	Deformation of the PBG Cavity	105
Table 5.1	Structural Parameters of Multi-Section RF Cavity	115
Table 5.2	Resonant Frequency, Quality Factors, Effective Length, and Frequency of the Multi-Section RF Cavity	115
Table 5.3	Resonant Frequency, Quality Factors, and Effective Length of the RF Cavity (For $\theta_2 = \theta_3 = \theta_4 = 0^\circ$, $L_2 = L_4 = 12$ mm)	120
Table 5.4	Design and Simulation Parameters of Gyrotron	121
Table 6.1	Design Parameters of 527 GHz Gyrotron	134
Table 6.2	Structural Parameters of 527 GHz Gyrotron	135
Table 6.3	Comparison of Deformation Obtained by ANSYS and Theory	144